

# Read-out of LYSO:Ce Matrix Detector using Wave-Length-Shifter fibers applicable to new PET Scanner with High Spatial Resolution at Low Cost

Souichirou AOGAKI<sup>1)</sup>

Fujio TAKEUTCHI<sup>2)</sup>

<sup>1,2)</sup> Faculty of Computer Science and Engineering,  
Kyoto Sangyo University, Kyoto, Japan

## Abstract

In building a PET scanner, crystal read-out using wave-length shifter fibers (WLS) permits the use of many small crystals with a reduced number of photo-sensors, thus promising good spatial resolution at low cost. However, the main drawback of this method has been low efficiency of photon collection. Improvements in design of our readout system over the last several years have resulted in a factor of more than ten in the collection of photons. In the present study, a narrow gamma-ray beam is injected to a matrix detector composed of  $16 \times 16$  LYSO:Ce crystals which are read out by using  $2 \times 16$  Kuraray Y-11 WLS fibers and two Hamamatsu H6568ModIII photomultipliers. A good spatial (0.34 mm RMS) and time resolution are obtained. The observed time resolution allows the use of 10 ns coincidence time window with a loss of 8.8%. A detection efficiency close to that of a single block LYSO crystal directly mounted on PM was obtained. A sketch of a full size animal PET scanner with 20 cm internal diameter is given. Building such a device by using the method developed in the present study needs only 54 photomultipliers identical to those used in this study.

## 1. Introduction

In this paper we report on the result of our study of read-out of scintillator crystal matrix detector using wave-length shifter fibers (WLS). The aim of the study is to explore the possibility of applying this read-out method to build a PET scanner comprising a large number of small crystals at low cost. We made a matrix counter with small scintillator crystals, and studied its response to the 511 keV gamma-ray from the view point of the spatial and time resolution as well as the detection efficiency.

Reading-out of a matrix detector using WLS was tried in the past [1-5]. The advantage of this method is that a WLS fiber can read out many crystals at a time and that it is possible to increase the number of crystals without increasing the number of photo-devices. This is because the number of needed photo-sensors in the case of two-dimensional read-out is proportional to the square root of the number of the crystals. High granularity of the detector makes the improvement of the intrinsic spatial resolution easier. The simplicity of the construction is another advantage. A drawback of this method, however, is that the number of read out photons is strongly reduced. Actually in our measurement in the past by using this method, the number of photons collected was only several, which resulted in poor detection efficiency. The reduced efficiency of the collection of photons also makes the pulse-height discrimination impossible. That means the quality of the obtained image might be poorer, although the higher granularity due to the use of a larger number of crystals can improve the quality of the image.

The loss of photons when WLS fibers are used occurs mainly at the joint of crystal and WLS fiber [5]. One of the causes of the loss is concerned with the geometrical matching of the crystal and WLS fiber whose role is to bend the photons by 90 degrees. Another is related with the difficulty of extracting the photons from the crystal end into the air when crystal has a high index of refraction. We have been working at solving these problems and have succeeded in obtaining as many as about 25 photoelectrons by using materials like LYSO:Ce crystal[6, 7] and Y-11 WLS fibers. This is satisfying from the view-point of the detection efficiency. In this paper, we report how good spatial and time resolution can be obtained by using this method. We will explain how we measured the photoelectrons, detection efficiency, etc., and also discuss possible future progress.

In this measurement we use  $1 \text{ mm} \times 1 \text{ mm} \times 20 \text{ mm}$  LYSO:Ce 0.04 wt% crystals that are totally polished. We pile them up to make a pad (matrix) without inserting light-insulating material between crystals and without applying pressure on the pad. Photons emitted in a small solid angle with respect to the central axis of the crystal are transported to the end of the crystal whereas those emitted with a large angle escape from the crystal and enter another crystal but keeping the initial emission angle. An interesting finding made is that with this angle, they appear not to be able to exit from the end point of the crystal. This means that they do not cause light cross talks between crystals. If that is the case, then construction of a large detector becomes easier, and we can gain the effective volume of the detector since we do not need any light-insulating material to be inserted between crystals.

The experimental setup and method are explained in Sec. 2. With a small radioactive source together with a thin scintillator, we made a "gamma-ray beam injector", and we irradiated the matrix detector with this beam. In Sec. 3 we examine the characteristics of this gamma-ray beam.

Light output from the tested counters is described in Sec. 4. Section 5 is devoted to the spatial resolution. We discuss the detection efficiency and the time resolution of the detector in Secs. 6 and 7, respectively. A summary and discussion are presented in Sec. 8.

## 2. Experimental setup and method

### 2.1 Setup

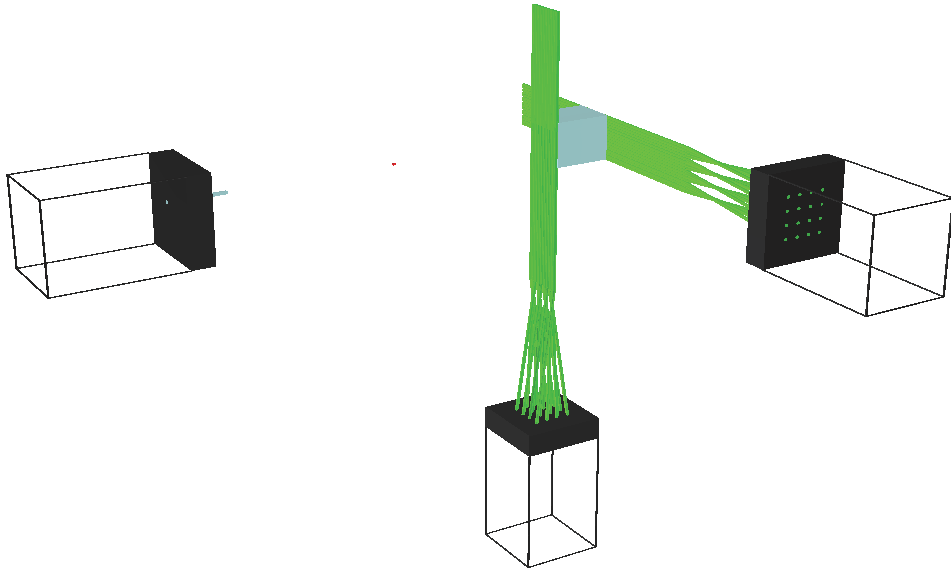


**Fig. 1** The experimental setup. The  $^{22}\text{Na}$   $\beta^+$  source is placed in the middle. The needle detector to the left and the matrix detector to the right are placed both at 120 mm from the source.

Figure 1 is a schematic view of the experimental setup used. There are two detectors, one to the left of the figure and the other to the right. At the mid-point between the two detectors, a gamma-ray source is placed. A pair of gamma-rays of energy of 511 keV are emitted back-to-back from the source. We use  $^{22}\text{Na}$   $\beta^+$  for the gamma-ray source, which is a sphere of 1 mm in diameter. The left detector is a scintillator crystal, which is a long parallelepiped of 1 mm  $\times$  1 mm  $\times$  20 mm in size. It is directly coupled to a photomultiplier (PM) by using optical grease (OKEN 6262A). It lies on the central axis that connects the two detectors. One of the 1 mm  $\times$  1 mm faces is directed towards the gamma-ray source. We call this detector a needle detector hereafter. The distance from this face of the detector to the gamma-ray source is 120 mm. The gamma-ray source together with the needle detector can be considered as a gamma-ray beam injector to the right-side tested detector [8-11]. The thickness of the beam as well as its angular divergence is determined by the

sizes of the source and the needle detector. We study the characteristics of the gamma-ray beam in Sec. 3.

## 2.2 The matrix detector

The tested detector which we call the matrix detector hereafter is placed on the right side in Fig. 1. To find out the performance of the matrix detector, the gamma-ray beam is injected to it using the gamma-ray beam injector we described in Sec. 2.1. This detector is a matrix (pad) that consists of  $16 \times 16$  parallel scintillator crystals, each of which is identical to the left detector. It is placed at the distance of 120 mm from the gamma-ray source. The crystals of this detector are all parallel to the central axis. (In reality, the central axis goes through the 8th crystal, counted from both ends.) All the surfaces of the crystals are totally polished. Each end, front and back, of the crystal arrays that form a matrix are connected to 16 WLS fibers which in turn are connected to 16 channels of the photocathode of a PM. The front 16 WLS fibers run vertically to read out the y position of the matrix, while the back 16 WLS fibers run horizontally to read out the x position. (Note that only 32 PM channels are used to read out 256 crystals.) One of the ends of each of the WLS fibers is connected to the photocathode of a PM. Sixteen holes ( $1.0 \text{ mm } \phi$ ) are drilled in a  $4 \times 4$  matrix form on a small black plastic piece ( $30 \text{ mm} \times 30 \text{ mm} \times 7 \text{ mm}$ ), the ends of the WLS fibers are put into the holes and then fixed with epoxy resin. The surface of the plastic piece is firmly pressed to the photocathode after being polished. A thin layer of optical grease is applied between the plastic piece and the photocathode. The other ends of the WLS fibers are cut perpendicularly to the central axis, polished, and small pieces of aluminized mylar are glued to the open ends by using the optical cement (OKEN BC-600) (The results obtained with a setup without using the mylar are already published[12]). For the PM we used two HAMAMATSU H6568 MOD III for the matrix detector. Each of the PMs has 16 independent channels. Special characteristics of this PM are: 1) It is equipped with ultrabialkali photocathode with quantum efficiency as high as about 41 % maximum. 2) Its uniform gain allows us to observe the single photoelectron peak clearly. We will discuss the latter point more in Sec. 4.1. The PM voltage divider is modified so that we can obtain the "last dynode" signal, which is the sum of all the output signals from the 16 channels.

We use Kuraray Y-11 as WLS fibers. Its double clad version has light transportation efficiency much higher than that of its single clad version. The double clad version, however, is commercially available only with round sections. Thus we have to use the cylindrically shaped WLS fiber of 1 mm in diameter to be placed the flat end of the crystals. The crystals are connected to WLS fibers by using an elastic film (0.125 mm thick). The insertion of this film and the removal of the air layer between the crystal and the WLS fiber eases the exit of photons from the crystal that has a

very high refractive index (1.82). Without the elastic film, the end of the crystal repels 93% of the photons transported to the end. Also this film is soft and, when a small pressure is applied, the surface that touches the round WLS fiber increases.

The emission peak of LYSO:Ce is at 440 nm in wavelength. The absorption and emission peaks of the WLS are, respectively, at about 430 - 460 nm and 470 - 500 nm. The maximum photosensitivity of the photocathode of the PM used is at about 350 - 400 nm. There is a small mismatch between the wavelength of the secondary emission from the WLS and the photocathode.

### 2.3 The block detector

In some cases the matrix detector on the right is replaced by a "block detector" which has the same size as the matrix detector, namely 16 mm  $\times$  16 mm  $\times$  20 mm but consists of a single block of LYSO scintillating crystal. All the surfaces are totally polished. The 16 mm  $\times$  16 mm face of the crystal is directly mounted onto the PM photocathode by using optical grease (refraction index: 1.45). We use this detector for two purposes. One is to compare the light output and the timing feature of this "quasi-ideal" detector with the matrix detector and the other is to use this detector as a control of the detection-efficiency measurement of the matrix detector discussed in Sec. 6.

### 2.4 Electronics and the data acquisition

A schematic view of the electronics with NIM and CAMAC modules used in this study is shown in Fig. 2. The trigger signal for the data acquisition is formed with the two last dynode signals from the right detector and the anode signal from the left detector in coincidence. All pulse-height of the anode signals from the PMs as well as their timing are recorded and digitized by means of an charge-sensitive analog to digital converter (14bits ADC; Hoshin C009-H) and a time to digital converter (TDC; Philips 7187) in a CAMAC crate, together with the last dynode signals from the right-side PMs. The CAMAC crate is interfaced to a computer via a VME crate by means of a Kinetics 3922 CAMAC crate controller, a Kinetics 2917 K-BUS INTERFACE, and VMEMM modules and a PCIADA computer board made by Wiener Plein & Baus Elektronik.

The data analysis has been carried out by using OMON program, which is developed on the basis of ROOT [13].

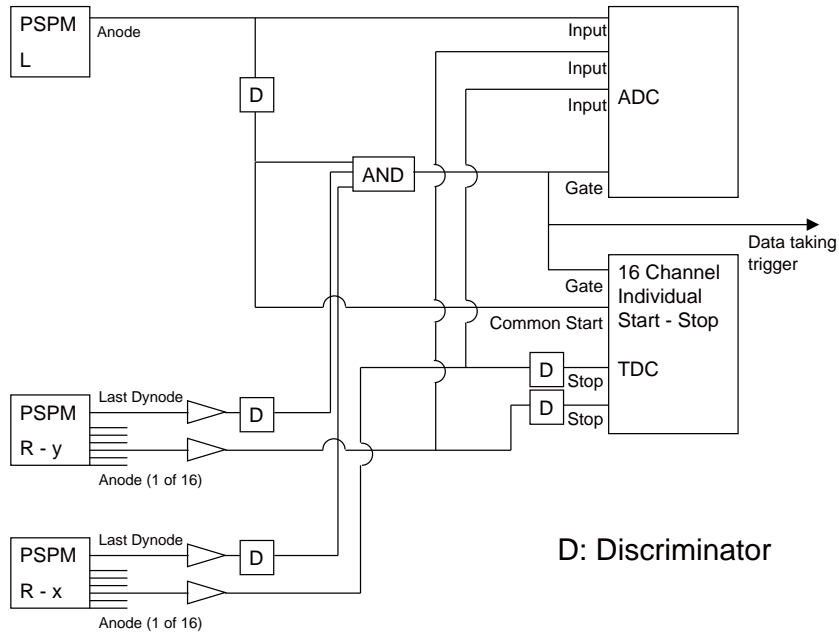


**Fig. 2** Schematic view of the electronics used for the data acquisition.

### 3. Characteristics of the gamma-ray beam

#### 3.1 Light output of the needle detector

Figure 3 shows the pulse height distribution obtained from the needle detector. This measurement is performed with the needle detector in coincidence with the matrix detector. The reason for doing so is that the LYSO crystal contains 2.59% of naturally radioactive isotope  $^{176}\text{Lu}$  in the lutetium component of the crystal, and its decay can contaminate the data. Also the  $^{22}\text{Na}$  source emits 1.28 MeV single gamma-rays in addition to the  $\beta^+$ . To suppress these background noises, it is necessary to make a measurement in coincidence with any detector placed on the opposite side. Although the photo-absorption peak is clearly visible in the spectrum, the Compton continuum is more enhanced than the photo-absorption peak. This feature must be due to the following reason. In the case of LYSO, if the crystal is sufficiently large, most of the gamma-rays will be absorbed via photo-absorption process, either directly or after one or two Compton scattering processes. This is because of its large effective  $Z$ . The left side detector, however, is very thin. Therefore, many of the gamma-rays Compton-scattered in the crystal exit from the crystal. This makes the Compton continuum larger. This can be confirmed by using an EGS simulation [14]. In the present study, we limit the events to those that are included in the photo-absorption peak of Fig. 3. This is in order to

be free from the threshold effect and also not to accept events in which gamma rays are scattered by any material before entering the needle detector.

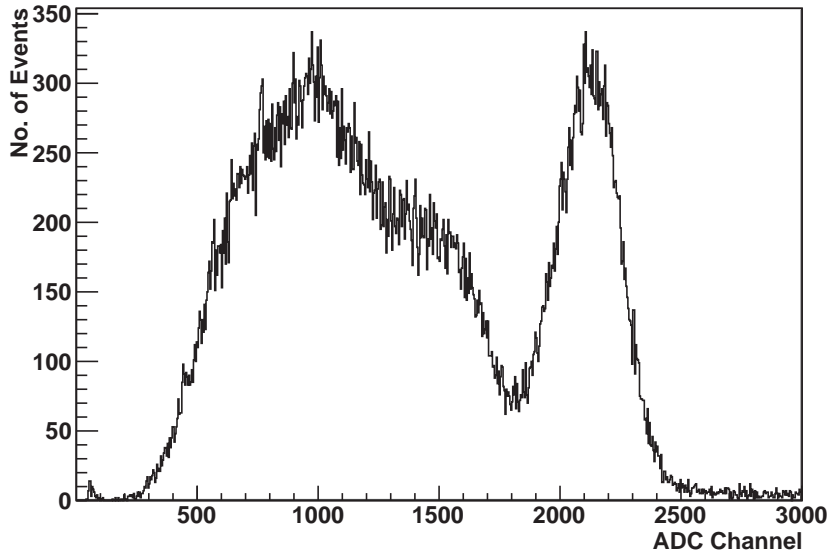


Fig. 3 Pulse height distribution obtained from the needle detector (ADC output) .

### 3.2 Thickness and the angular divergence of the gamma-ray beam

To determine the thickness of the gamma-ray beam experimentally, we have carried out a subsidiary measurement in which we scan the intensity of the gamma-ray beam as shown in Fig. 4. The crystal matrix of Fig. 1 is replaced by a single crystal of  $1\text{mm} \times 1\text{mm} \times 20\text{mm}$  in size, which is directly connected to a PM. This crystal is kept vertical and perpendicular to the crystal of the needle detector to the left. The right detector is moved horizontally stepwise with a step of  $0.5\text{mm}$ . We record the fraction of the coincident events among the left counter events. For the detector to the right we vary its position over nine different positions. Figure 5 shows a graph of the spread of the gamma-ray beam. The vertical axis indicates the number of counts of coincidence events.

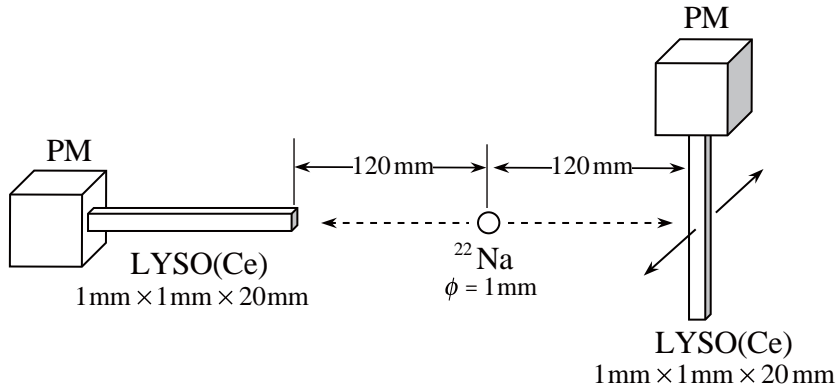


Fig. 4 Setup of the subsidiary measurement.

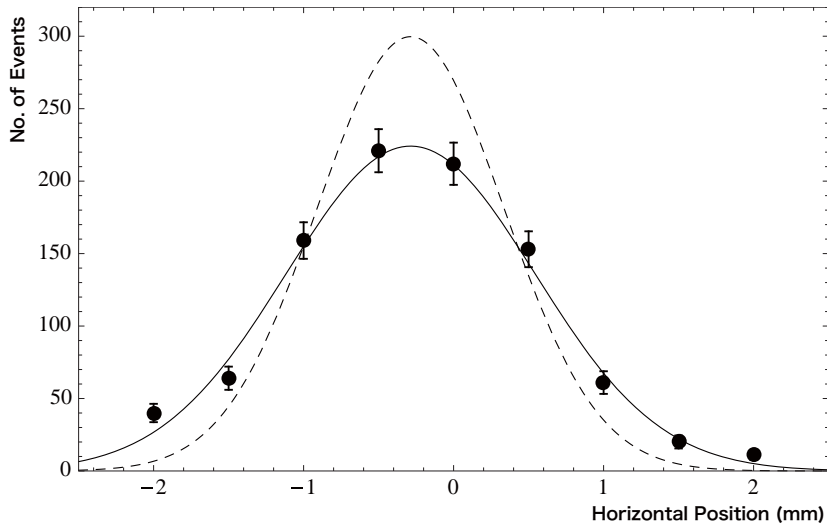


Fig. 5 Spread of the "gamma-beam". The solid line reproduced the data. The dashed line represents the simulation without the diffuseness.

In order to find the angular spread of the gamma-rays also (namely the phase space occupied by the gamma-rays in the beam), we develop a simulation program in which the source of the gamma-ray is a uniform sphere with a diameter of 1.0 mm. It is, however, found not possible to reproduce the measurement with this "perfect source", even by introducing possible misalignment of the needle detector, or slight dilatation of the sphere. We then assume that the surface of the sphere is diffuse by introducing a Wood-Saxon type diffuseness parameter. The idea behind it is that the  $\beta^+$  emitted in the decay has a relatively large kinetic energy as large as  $E_{\text{max}} = 540\text{ keV}$ . Therefore, the annihilation can take place well outside of the plastic sphere, either in the air, or in the surrounding plastic material [15]. Also, even if the annihilation takes place inside the sphere,

the positron may be in flight, and the two gamma-rays may not be emitted perfectly back-to-back. This phenomenon makes the effective source larger. We keep the radius of the source sphere to be 0.5 mm and vary the diffuseness parameter. The result with the diffuseness of 0.14 mm, drawn in Fig. 5 with a solid line, reproduces the data the best. The dashed curve in the figure represents a simulation without the diffuseness. The result of the simulation gives the spread in position of 0.77 mm RMS and in angle of 3.6 mrad RMS at a distance of 120 mm, that means where the matrix detector is placed in the coincidence experiment.

## 4. Light output from the tested detectors

### 4.1 Light output from the block detector

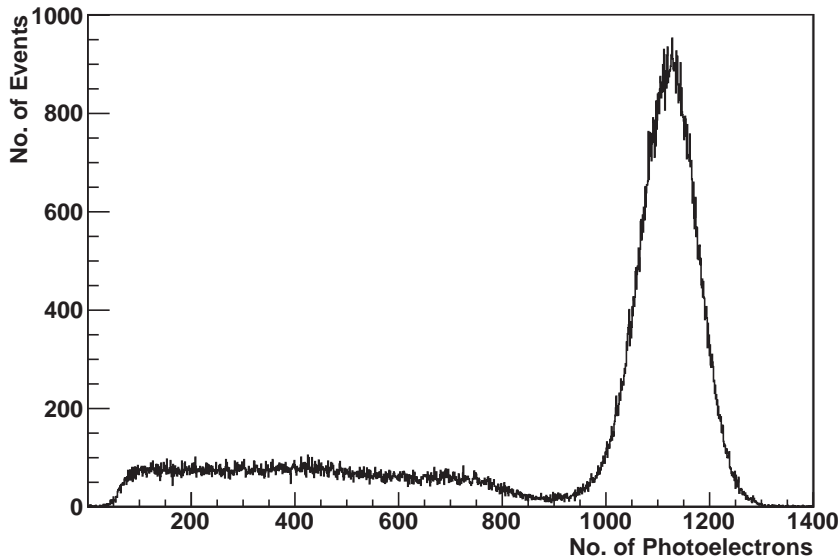


**Fig. 6** Light output (ADC) distribution from the crystal block directly mounted on the PM.

Figure 6 shows the sum of the ADC outputs of the block detector when it is irradiated with the gamma-ray beam. The threshold of the discriminators is set as low as -15 mV so that one can observe a peak corresponding to a single photoelectron peak. It is known that this PM has a cross talk of the level of the single-photoelectron peak through the photocathode window glass [16]. That means that even when there is no signal in one channel, the light leak from a near-by channel (near-by on the  $4 \times 4$  photocathode) creates the single photoelectron peak. This phenomenon, otherwise a nuisance, helps us to determine precisely the position of the single photoelectron peak because the uniformity of the gain in the first dynode area makes this peak very narrow. Thus the position of the single photoelectron peak can be determined for each channel, and the gain of each channel

(PM + preamplifier + ADC) can be normalized. The spectrum shown in Fig. 6 is produced as a sum of the ADC outputs normalized in this manner. All the spectra shown hereafter are displayed in terms of the number of photoelectrons. It should also be noted that for the reason stated in Sec. 3.1, the spectrum shown in Fig. 6 is obtained in coincidence with the needle detector.

In this spectrum, the photo-absorption peak is predominant. By fitting it with a Gaussian distribution, it was found that the peak position is at 1128 and the width is 54.62 RMS (125 FWHM) photoelectrons. The average number of photoelectrons obtained is 920. Assuming the quantum efficiency of the PM photocathode to be 40%, 2300 photons are estimated to reach the photocathode. On the other hand, according to EGS, the average energy deposit in this crystal of the gamma-ray is 465 keV. If we use the known photon output of LYSO crystal, which is  $\sim 25000/\text{MeV}$  [6], we find that about 10000 photons are produced in one event. We have done a simulation of the photon transport inside the crystal assuming that the surfaces of the crystal are perfect, neglecting the attenuation inside, and have found that 24% of the photons reach the photocathode, which gives 2400 photons. This is very close to the above-mentioned value of 2300 and one can conclude that the simulations are reasonably reliable.

#### 4.2 Light output from the matrix detector

Figures 7 and 8 show the pulse-height spectrum of the y-plane WLS fibers and that of the x-plane WLS fibers, respectively, of the matrix detector irradiated with the gamma-ray beam. They are also obtained in coincidence with the needle detector signal for the reason stated in Sec. 3.1.

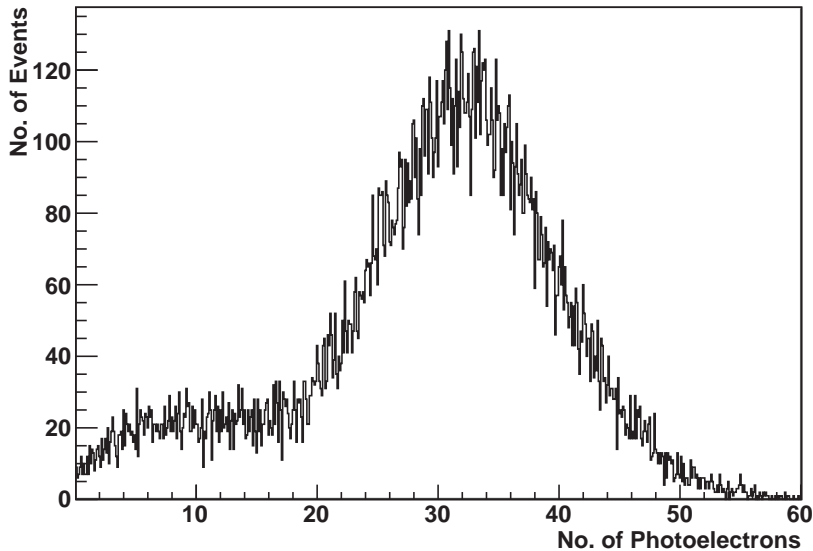


**Fig. 7** Histogram of all the ADC outputs of the y-plane WLS fibers added. The average number of photoelectrons is 29.3.

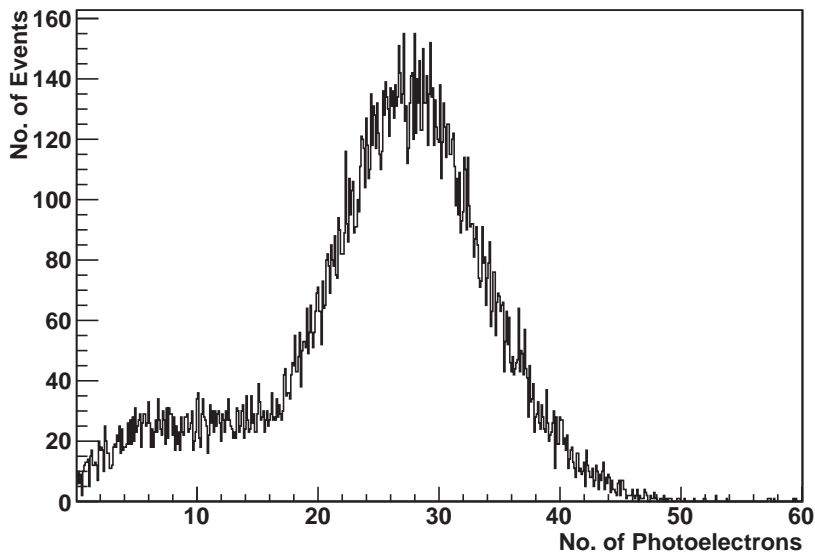


**Fig. 8** Histogram of all the ADC outputs of the x-plane WLS fibers added. The average number of photoelectrons is 25.2.

Note that the photo-absorption peak is no longer seen as an isolated peak in both of the spectra. This is due to the large attenuation of the photons. It should be noted that the average number of photoelectrons is 29.3 in Fig. 7 for y-plane, and is slightly smaller in Fig. 8 for the x-plane, which is 25.2. This difference can be understood as follows. In a separate measurement, it was found that the attenuation of the emitted light within the needle counter along the length is as large as  $\mu = 0.79 / \text{cm}$ , where the attenuation is expressed as  $e^{-\mu x}$ ,  $x$  being the path along the crystal. Since the number of the absorbed gamma-rays in the crystal decreases exponentially as the length of the crystal increases, there are more absorption near the front side y-plane WLS fibers. Consequently the average pulse height is larger than that in the backside x-plane WLS fibers.

With the matrix detector, the photon transmission after the exit from the crystal is lower than in the case of direct mounting. This is mainly due to the conversion of primary photons to the secondary ones produced in the WLS, but also due to fact that the WLS fiber is cylindrical. A simulation of the transport of photons from the crystal surface to the WLS fiber core through the film and the WLS fiber core and a simulation of the secondary photons produced inside WLS fiber up to the photocathode have been performed. Comparison of the number of photons in each stage, estimated and observed, is shown in Table 1. The estimated number of photoelectrons in the case of the matrix detector is 19 and the agreement with the experiment is found to be very good. It is found that the spectrum shown in Fig. 6 decomposed into Poisson distributions, and the sum of the Poisson distributions with the means multiplied by the attenuation factor (either 29.3/920 in the

case of y-plane, and 25.2/920 in the case of x-plane) reproduces very well the spectra shown in Figs. 7 and 8, respectively<sup>1</sup>. This demonstrates that, although the attenuation of photons is substantial with the use of WLS fibers, the fluctuation of the attenuation is small.

Stages	Directly mounted block	Matrix detector using WLSs
Average energy deposit within the 16mm × 16mm × 20mm LYSO crystal	465keV	465keV
Average number of photons produced	10000	10000
Number of photons exiting the LYSO crystal. (Simulation)	2400 (LYSO to optical grease)	780 (LYSO to air)
Number of photons reaching photo-cathode of PM.	2400	47
The number of photoelectrons (Simulation)	960	19
The number of photoelectrons (Observed)	920	21.7 (y-plane) 17.4 (x-plane)

**Table 1** The number of photons and photoelectrons at each step, simulated and observed. In this simulation, aluminized mylars are not glued to the ends of WLS fibers.

## 5. Spatial Resolution of the matrix detector

Assume an idealized situation in which an infinitely thin gamma-ray beam is injected to the center of one of the central crystals in the matrix detector. If the spatial resolution of the right detector is ideally good (e.g., no light cross talk, etc.) , then all the hits will be recorded in the central crystal, (in our case,  $x = 9, y = 8$ ) and the apparent spatial resolution would be simply  $1/\sqrt{12} = 0.29$  mm (RMS) since we do not know which part of the crystal is hit. In reality, the matrix detector has a finite spatial resolution, which makes the distribution broader. This is mainly due to the gamma-ray Compton-scattered in the central crystal and photo-absorbed by one of the adjacent crystals. (When a far-apart-pair of crystals are hit, then the event itself is rejected to minimize the Compton effect.) The cross talk at the level of the crystal-WLS fiber joint also makes the spatial distribution broader. The film between the crystal and WLS fiber may be partially responsible for

<sup>1</sup> This slightly complicated statement is more easily understood by using formulae.

The pulse-height distribution of the block detector, shown in Fig. 6 is denoted by  $B(n)$  as a function of number of photoelectrons  $n$ . It is decomposed to the Poisson distribution  $P(n; \mu)$  with parameter  $\mu$  as its mean.

$$B(n) = \int b(\mu) P(n; \mu) d\mu,$$

where  $b(\mu)$  is the weight of each component. Let us assume that the attenuation factor (in this case 29.3/920 or 25.2/920) be  $a$ . Then the statement is that the distribution of the pulse-height distribution  $M(n)$  of the matrix detector shown in Figs. 7 or 8 can very well be described as

$$M(n) = \int b(\mu) P(n; a\mu) d\mu.$$

the spread. Also there could possibly be a light cross talk within the crystal matrix, and also at the level of the WLS fibers [16]. Events are accepted in which one WLS fiber receives most of the light, but in addition, those in which one WLS fiber records the maximum amount of light whereas two adjacent WLS fibers receive fractions of light. The WLS fiber recording the maximum amount of light is assigned as the “hit” array in our analysis. The hit array determined by x-plane WLS fibers and that determined by y-plane WLS fibers define the “hit crystal”. We define the spatial resolution of a detector as the spread in the histogram of the hit crystals in the case where the injected beam is infinitely thin and call that the intrinsic spatial resolution of the detector. This is an important figure of merit, which characterizes the quality of the detector. This, however, cannot be measured directly since the thickness of the gamma-ray beam is not small compared to the size of the crystal. The spread of the image of the actual gamma-ray beam obtained with the matrix detector is a convolution of the detector’s intrinsic spatial resolution (uncertainly) and the thickness of the gamma-ray beam. We need to deduce the intrinsic resolution from the observed spread of the gamma-ray beam image using the information of the beam obtained in Sec. 3.2. We will describe first the observed distribution with the real gamma-ray beam in the next section, and then the process of obtaining the intrinsic resolution and the result in Sec. 5.2. In Sec. 5.3 we will show that the obtained intrinsic resolution so obtained is not specific to the center of the matrix detector but rather it is constant everywhere inside the matrix.

### 5.1 Experimentally observed spread of the beam image

The matrix detector is irradiated at its center with the gamma-ray beam. Figure 9 shows a box plot of the 2D histogram of hit crystals obtained by means of the crystal matrix in the coincidence measurement. In this plot, a box is drawn for each bin with an area proportional to the bin contents (the number of events). The vertical and horizontal axes are the x and y axes, respectively, associated with the crystal matrix. The binning is chosen so that one bin corresponds to one crystal in the matrix.

Figure 10 shows a plot of events distribution, which is a 1mm slice of the above 2D histogram along  $y = 8$ . The vertical axis refers to the number of events shown together with error-bars corresponding to the square root of the number of the events in the bin, whereas the horizontal axis is the x-coordinate of one row of the crystal matrix with a step of 1 mm. This graph can be fitted with logistic distribution<sup>2</sup> with a width of 1.03 mm (RMS, or 2.25 mm in FWHM) shown with a dotted curve.

---

<sup>2</sup> This rather “unusual” distribution instead of Gaussian distribution is used here since it gives noticeably smaller  $\chi^2$  value for some reason than Gaussian distribution. In reality the two distributions have fairly similar shapes. The width given here is the standard deviation of the logistic distribution, which is  $\pi/\sqrt{3}$  times its parameter  $\beta$ .

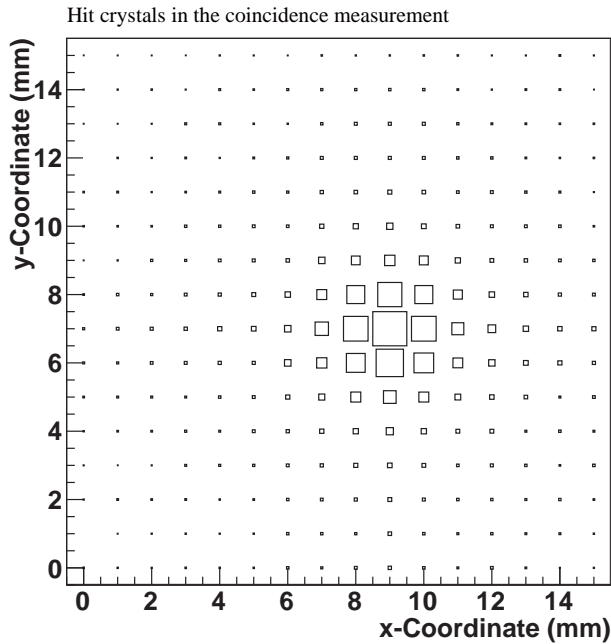


**Fig. 9** Box plot of the 2D histogram of hit crystals obtained by means of the crystal matrix in the coincidence measurement. In this plot, a box is drawn for each bin with area proportional to the bin contents (number of events). The vertical and horizontal axes are the x and y axes, respectively, associated with the crystal matrix. The binning is chosen so that one bin corresponds to one crystal in the matrix.

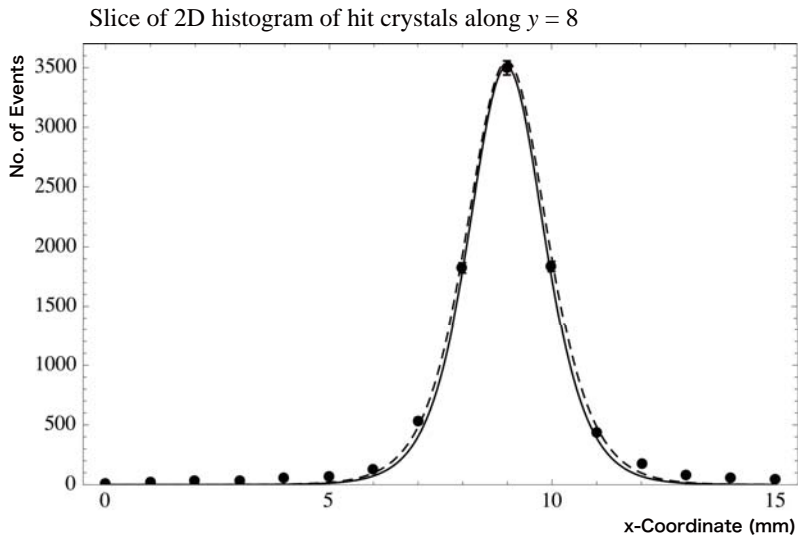


**Fig.10** Plot of events distribution in the 1mm slice along  $y = 8$  of the 2D histogram shown in Fig. 11. The vertical axis refers to the number of events shown together with error-bars corresponding to the square root of the number of events in the bin, whereas the horizontal axis is the x-coordinate of one row of the crystal matrix with a step of 1 mm.

## 5.2 Intrinsic spatial resolution of the matrix detector

On the basis of the information concerning the gamma-ray beam, and using the developed code, we try to deduce the intrinsic spatial resolution of the matrix detector. Roughly speaking, we can obtain the intrinsic spatial resolution by quadratically removing the width of the gamma-ray beam (0.77 mm RMS) from the observed spread of the gamma-ray beam (1.03 mm RMS), which gives 0.68 mm RMS. This value so obtained cannot be quite right, since the hit position of the gamma-ray and its angle are not random but correlated. To understand better what causes this intrinsic resolution, we make the following exercise. First, by using EGS simulation program we inject a 511-keV gamma-ray to a wide LYSO scintillator slab with a thickness of 20 mm and record the photon emission at all the interaction points in the crystal (Compton scatterings and photo-absorption). We repeat this procedure by varying the injection angle, and make a large database. Then we inject gamma-rays randomly within the known phase space to the 16 x 16 matrix detector. We count the number of photons emitted in each crystal, which are totally reflected on the inter-crystal surface, and successfully exit from the end point of the crystal. We accept/reject each event according to the criteria mentioned in Sec. 5, and calculate the hit distribution. The result is shown with a solid curve in Fig. 10. One can see that this result reproduces very well the experimentally observed distribution. This model gives 0.34 mm RMS (or 1.0 mm FWHM) as intrinsic spatial resolution and we designate this value to be the most probable intrinsic spatial resolution of the matrix detector.

It should be noted that in this simulation, we assume that the photons fulfilling the angular condition are perfectly totally-reflected at the side surface of the crystal, and the escaped photons to the adjacent crystals may reach the endpoint of the crystal, but cannot exit from it, and hence make no cross talk as mentioned in the introduction. If this assumption were not right, then the observed distribution should be broader than the one calculated. The fact that this model reproduces well the experimental observation strongly supports that the assumption made is plausible. We make also a simulation of the transport of photons through the transparent sheet, and in WLS fiber, but not included in the shown curve for the clarity.

## 5.3 Uniformity of the spatial resolution within the matrix detector

We make a test of readout of many small crystals with WLS fibers using a matrix of only 16 x 16. But our aim is to find if this readout method is applicable to a larger detector composed of the same crystals. Thus if the good intrinsic resolution is obtained only in the center of the matrix, or if the outer walls of the matrix play any role in the resolution, then its significance of the obtained intrinsic spatial resolution is restricted. We therefore try to examine if the spatial resolution is

uniform within this matrix. In this purpose we scan the detector with the gamma-ray beam along the line  $y = 8$ , with a step of 2 mm. The result, namely the slice plots similar to the one shown in Fig. 10 together with fit to each peak, are presented in Fig. 11. One can see that the spatial resolution is almost constant, and there is no special effect coming from the walls.

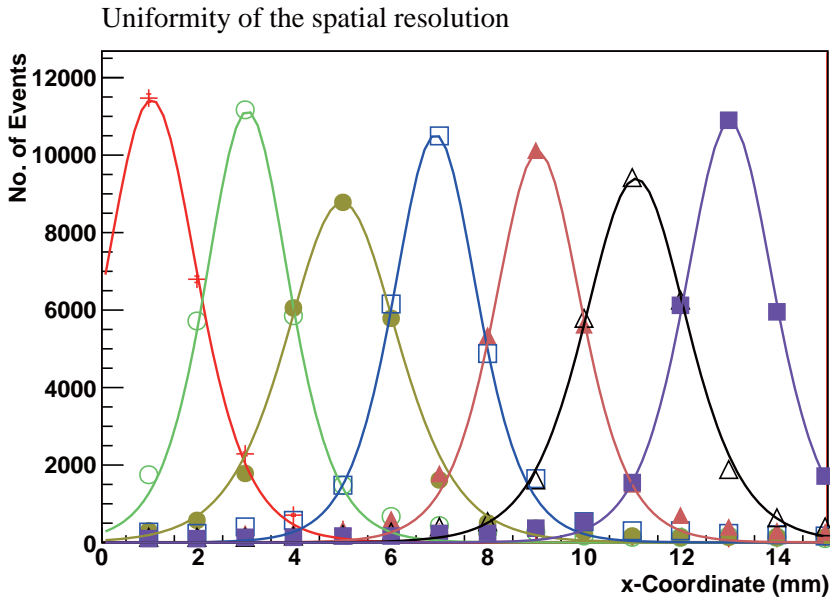


**Fig. 11** Slice plots similar to the one shown in Fig. 12 together with fit to each peak. The matrix detector is scanned along  $y = 8$  to check the uniformity of the spatial resolution.

## 6. Detection efficiency

In the EGS simulation, one finds that the detection efficiency of 511 keV gamma-ray with a LYSO:Ce scintillator with a thickness of 20 mm is 81%. This is the absolute maximum one can expect for the matrix detector. A question that arises here is; what fraction of this 81% the efficiency of the matrix detector is. Since we have seen that the reduction of the number of photoelectrons compared to the direct read out is almost constant, we can expect a good detection efficiency even for the matrix detector. Nevertheless it is important to find this fraction experimentally, hence we make measurements of the coincidence rate using the matrix detector and the block detector in place of the matrix detector and compare the results. The distances between the source and the right-side detectors are all identical in the two cases. To avoid accidental coincidence events, a cut is applied on the left-right time difference to 16 ns in both cases. Out of 100000 triggers, which are made only with the left-side needle counter, the number of coincident events with the block detector

is 4155 whereas with the matrix detector, it is 4191. Figure 12 shows the ADC spectrum obtained from the matrix detector. Since the signal from the matrix detector is not put in the trigger signal in this measurement, one notices a small surplus of events at very low pulse heights. To be more realistic, events with a very small pulse height on the right-side detectors ( $< 5$  for the matrix,  $< 118$  for the block) are omitted from the analysis. After this pulse-height cut, the number of events are found to be 4074 with the block detector, and 3927 with the matrix detector. Thus the fraction mentioned above is found to be  $0.964 \pm 0.001$ . The results are summarized in Table 2. One can conclude that the efficiency of the matrix detector read out with WLS fibers is by no means much inferior to that of the block detector, and the counting efficiency for the 511 keV gamma ray is about 78% in absolute value.

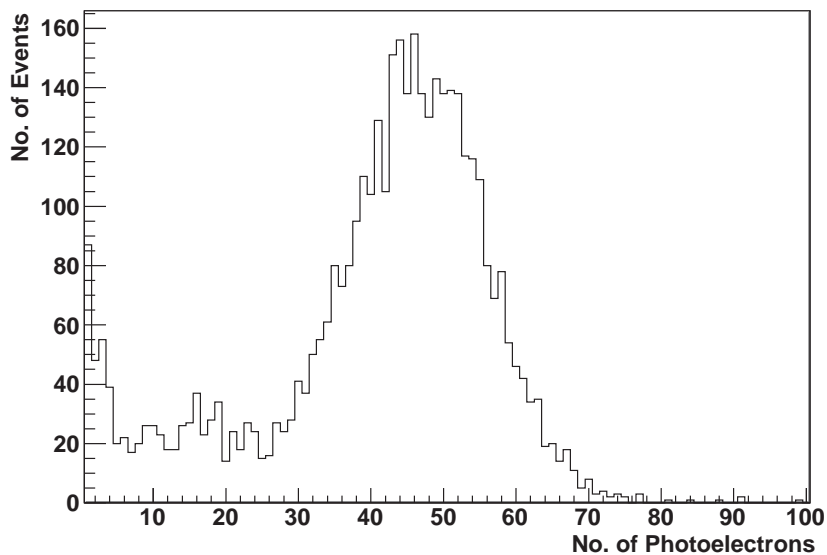


**Fig.12** ADC spectrum from the matrix detector. Sum of x- and y-planes.

	Block detector	Matrix detector	Ratio
Number of all events	100000	100000	1.0
Number of coincident events (with TDC cut)	4155	4191	$1.009 \pm 0.001$
Number of coincident events (with TDC and ADC cuts)	4074	3927	$0.964 \pm 0.001$

**Table 2** Summary of the evaluation of the detection efficiency measurements

## 7. Time resolution

Good time resolution is crucial for the PET that requires a high event rate, in order to identify the pair of gamma-rays from one beta decay among many hits. Good time resolution permits us to use a narrow time window (gate), and therefore allows a detection with a high event rate.

As the time resolution is mainly affected by the statistical fluctuation, it is strongly influenced by the number of photoelectrons obtained. Because the read-out of the scintillator using WLS fibers limits the collection of the light as already mentioned, it is important to obtain information on the time resolution that we can expect with the use of WLS fibers.

To determine the time resolution, we measure the time difference between the needle detector to the left and the matrix detector to the right. The timing of the matrix detector is, as can be seen in the electronic scheme, determined by the earlier of the two planes x and y, and also the earliest timing among the WLS fibers of that plane. In addition, the time difference between the x- and y-planes was measured. Also we replace the matrix detector by the block detector which gives a very good photon yield as we saw in Sec. 4.1. We then measure the time difference between the needle detector and the block detector in order to evaluate the uncertainty that stems from the circuitry and the PM itself.

Philips 7187 CAMAC TDCs are used for the measurement. The time resolution of this device is 25 ps/channel with the range of 100 ns. Sixteen WLS fibers from each plane are mapped on the photocathode of a PM. The timing signal was taken from the 16 anode signals temporally aligned and calibrated. Due to the small size of the PM the shift for the timing alignment is almost unnecessary.

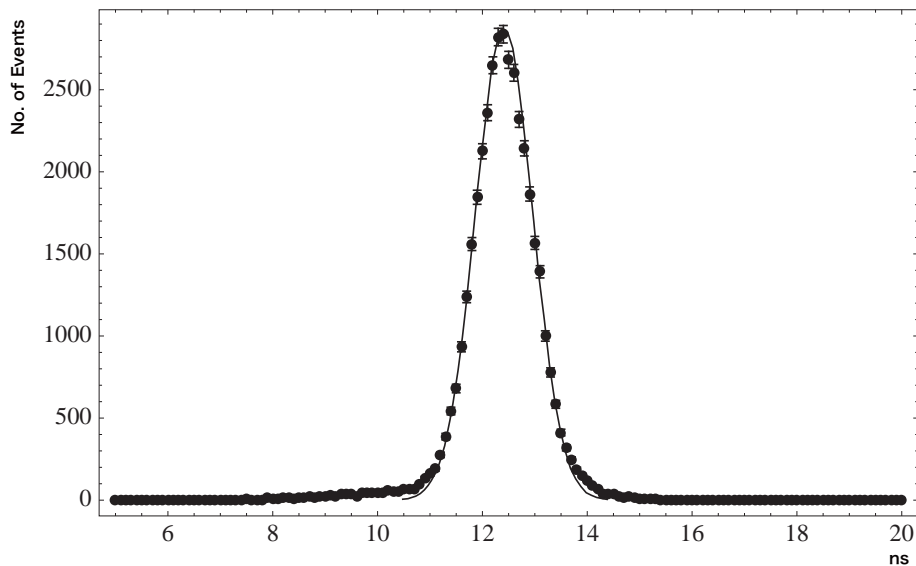
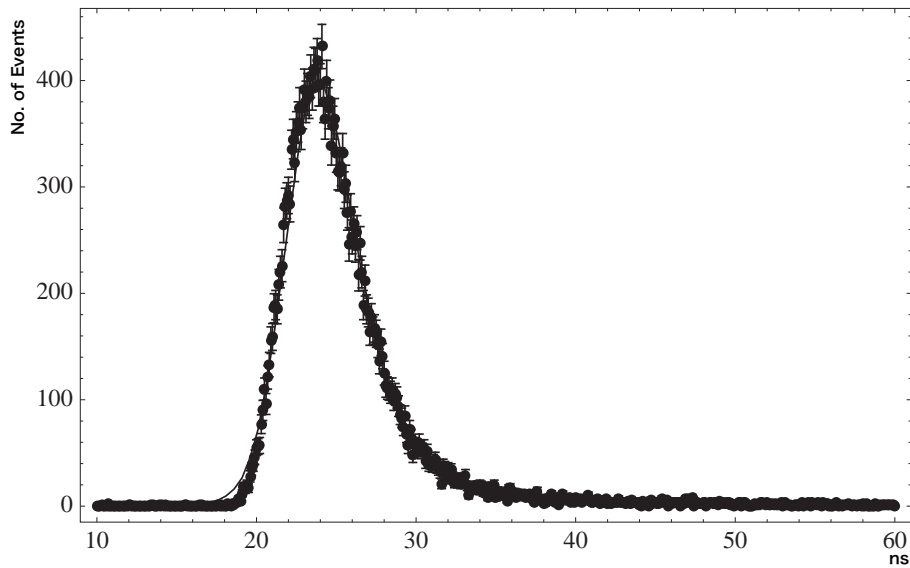


**Fig.13** Start: left needle detector, stop: block detector mounted directly on the photocathode of PM 6568 MODIII. For the curve, see text.

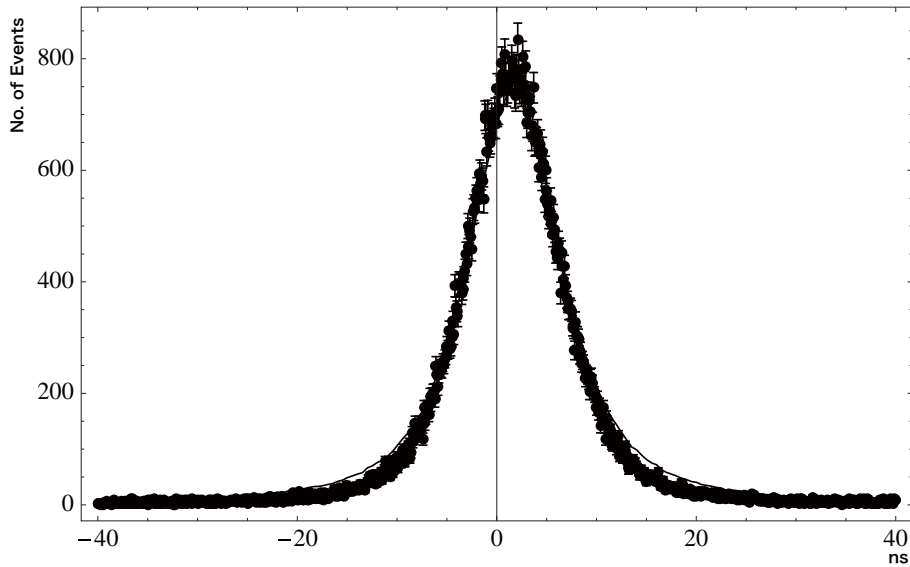
Figure 13 shows the distribution of the timing differences when the LYSO block detector is placed on the right side. The width of the peak is as small as 1.28 ns FWHM, but this is due to the large number of photoelectrons, about 700/event on the left needle detector, and about 960/event on the block detector. The estimation of the number of photoelectrons is given in Sec. 3.

Figure 14 shows the distribution of the time differences between the needle detector to the left and the matrix detector to the right. The width is 5.4 ns FWHM, and the distribution shows a long tail on the stop side due to the limited collection of light in the matrix detector.

A simulation is performed using the distribution of the photoelectrons obtained in Sec. 4. In this simulation, information about the fluctuation coming from the circuitry and the PM is needed. By assuming that this distributes normally with a standard deviation of  $0.194 + 5.5 / \sqrt{N}$  ns one could reproduce the best Figs. 11 and 13 simultaneously ( $N$  stands for the number of photoelectrons).



**Fig. 14** The distribution of the time difference between the left needle detector (start) and the right matrix detector (stop). The long tail on the right side is due to the limited number of photoelectrons from the matrix detector. See text for the curve.



**Fig. 15** The distribution of the time differences between x- (stop) and y- (start) planes are plotted. The FWHM is 11 ns. See text for the curve.

The time difference measured between x- and y- planes is plotted in Fig. 15. One observes a fairly long tail on both sides due to the limited collection of the light. The width of the distribution is about 11 ns FWHM. The simulation program produced to explain Figs. 11 and 13 also reproduces

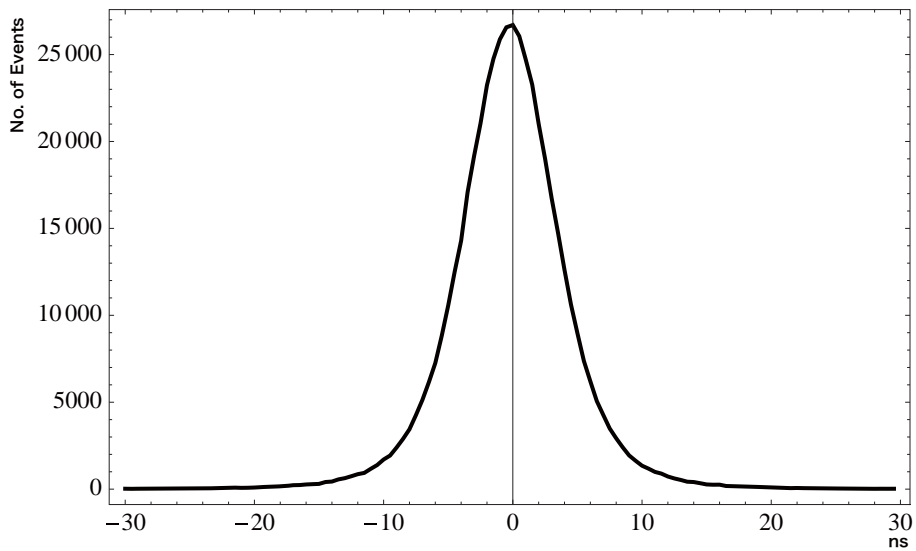


**Fig.16** Estimated timing fluctuation between two matrix detectors, in case such detectors are implemented in an actual PET scanner.

fairly well the distribution in Fig. 14, which justifies the plausibility of the model. On the basis of this simulation study, we estimate the timing fluctuation between two matrix detectors, which is the key factor for us in case such detectors are implemented in an actual PET scanner. Figure 16 shows the simulation of the variation of time differences between two of the identical matrix detectors. This figure tells us that even the time window (gate that discriminates the timing difference between the earlier and later signal) is narrowed up to 10 ns or 15 ns, we reject 8.8 % or 1.6 % of the coincident events, respectively.

## 8. Discussion and conclusions

The characteristics of the matrix detector read out using the WLS fibers have been investigated. The results are summarized in the following table.

Collected amount of light	Photoelectrons 29.3 (y-plane) , 25.2 (x-plane)
Detection efficiency	Almost the same as one single block of thickness 20 mm mounted directly to PM
Spatial resolution	0.34 mm RMS (1.0 mm FWHM) . Independent of the position
Time resolution	Time difference between the needle detector: 5.4 ns HWHM

Compared with our past result [5], the number of photoelectrons is much improved. This amount, 29.3 or 25.2, corresponds to about 1/34 of the direct read-out. The spatial resolution has been obtained by restituting the broadening due to the width of the “gamma-ray beam”. As for the time resolution, it is found that if such a detector as the current matrix detector is used in an actual PET, the detection loss due to the time window will be 8.8 % (or 1.6%) provided that a time window of 10 ns (15 ns) is applied.

It was found that the attenuation of the number of photons due to the use of WLS is almost constant, that is, it does not vary much from event to event. This is demonstrated by the fact that the pulse-height spectrum obtained from the block detector, decomposed into Poisson distributions, and the sum of the Poisson distributions with the means multiplied by the attenuation factor (either 29.3/920 in the case of y-plane, and 25.2/920 in the case of x-plane) reproduces very well the spectra obtained with the matrix detector (see footnote of Sec. 4.2). The fact that the attenuation does not vary explains the observation that the detection efficiency of the matrix detector is almost the same as that of the block detector. We see that the attenuation of the number of photons broadens the total absorption peak in the pulse-height spectrum. The value of the ratio  $\Delta E/E$  is 11% with the block detector (Fig. 6), where  $\Delta E$  is the FWHM of the total absorption peak, whereas it is about 45% for the matrix detector (see Fig. 12). This difference can be accounted for by the calculation mentioned above.

An extensive simulation of the photon production and its transport in the detector was performed using EGS code. The result was proven to reproduce many aspects of the experimental results and the reliability of the simulation was confirmed. One of the main conclusions derived from this is the confirmation of the statement we made in Sec. 1 that even without light-insulating material inserted between crystals, photons emitted with large angles with respect to the central axis do not cause light cross talks between the crystals. In fact, in the past, we built matrix detectors with different materials inserted between crystals and tested them. The spatial resolution obtained using 0.11 mm thick black flock paper inserted between crystals was almost identical to the one we observed in the present study. Insertion of such material, even thin, can reduce the effective volume of the matrix and therefore the detection efficiency, and also makes the

construction of PET scanners less easy.

This method of read-out of the crystal matrix by using WLS fibers may now be considered as applicable to the construction of a real device. Figure 17 shows a sketch of an animal PET scanner with an internal diameter of about 20 cm and an axial length of about 23 cm. This PET scanner comprises 135,680 scintillator crystals of size  $1\text{ mm} \times 1\text{ mm} \times 20\text{ mm}$ , but they can be read out only with 864 WLS fibers and 54 PMs that we used in the present study. In the figure, 32 out of 864 WLS fibers namely 16 inside the crystal matrix and 16 outside are drawn with red and green lines, respectively. To the ends of the 16 WLS fibers, one PM is attached. As the  $1\text{ mm } \phi$  WLS fiber is flexible, there is no problem in connecting 27 PMs on each side of the scanner. As the attenuation length of the Kuraray Y-11 WLS fiber is typically 3.5 m, the length of each WLS fiber of about 400 mm should not cause any problem. In this model, the readout is performed with 54 PMs for the reduction of costs. If we double the number of them and connect them to both ends of WLS fibers, the collected light will be almost doubled, and the resolutions will be improved with respect to the results of the current study.

If one uses LYSO:Ce crystals in the construction, a minimum length for the crystal of about 20 mm would be needed for a good detection efficiency. For such a PET scanner as the one with a diameter of 20 cm, the degradation of the spatial resolution at the limit of FOV (field of view) will occur. It, however, will be possible to obtain the DOI information from the ratio of the light output from each side of the crystal. (As already mentioned, the light attenuation length is about 7.4 mm). Du et al. reports on the DOI resolution of 6 mm FWHM in a read-out of LSO crystal ( $1.5\text{ mm} \times 1.5$

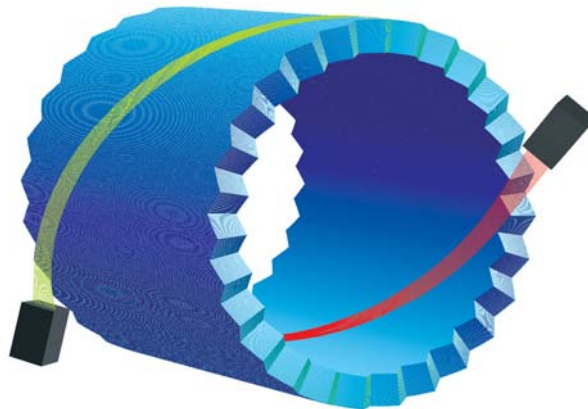


**Fig.17** Sketch of an animal PET scanner with an internal diameter of about 20 cm and an axial length of about 23 cm. This PET scanner comprises 135,680 scintillator crystals of size  $1\text{ mm} \times 1\text{ mm} \times 20\text{ mm}$ , but they can be read out only with 864 WLS fibers and 54 PMs. Sixteen WLS fibers out of 432 inside the crystal cylinder, and also outside are drawn with red lines. A 16 channel PM is attached to each end of the 16 WLS fibers of the matrix detector.

mm  $\times$  20 mm) using WLS fibers [2]. Although their crystal preparation is slightly different from ours, their result agrees with the preliminary measurement we made earlier using LYSO:Ce crystal of the current size. We plan to make a more detailed study on the DOI resolution.

### Acknowledgements

The authors are grateful to Professor F. M. Toyama for his constant encouragement. This work has been supported by the Science Research Promotion Fund from the Promotion and Mutual Aid Corporation for private School of Japan, and a grant from Research Institute of Advanced Science and Technology, Kyoto-Sangyo University.

### References:

- [1] D. J. Herbert, L.J. Meng, M. Dallimore, and D. Ramsden, Nuclear Science Symposium Conference Record **3** (1999) 1304-1308.
- [2] H. Du, Y. Yang and S. Cherry, Phys. Med. Biol. **52** (2007) 2499-2514
- [3] H. Du, Y. Yang and S. Cherry, Phys. Med. Biol. **53** (2008) 1829-1842.
- [4] A. Braem, E. Chesi, C. Joram, A. Rudge, J. Séguinot, P. Weilhammer, R. De Leo, E. Nappi, W. Lustermann, D. Schinzel, I. Johnson, D. Renker, and S. Albrecht, Nucl. Instr. Meth. A **586** (2008) 300-308.
- [5] F. Takeuchi, S. Aogaki, in Proc. 8th Intern. Conference on Inorganic Scintillators and Their Applications SCINT2005 (2006) 298-302.
- [6] C. M. Pepin, P. Bérard, A. L. Perrot, C. Pépin, D. Houde, R. Lecomte, C. L. Melcher, and H. Dautet, IEEE Trans. Nucl. Sci. **NS-51** (2004) 789-795.
- [7] A. Nassalski, M. Kapusta, T. Batsch, D. Wolski, D. Mockel, W. Enghardt, and M. Moszynski, IEEE Trans. Nucl. Sci. **NS-54** (2007) 2823-2829.
- [8] W. W. Moses, S. E. Derenzo, C. L. Melcher, and R. A. Manete, IEEE Trans. Nucl. Sci. **NS-42** (1995) 1085-1089.
- [9] P. Anfré, C. Dujardin, J.M. Fourmigué, B. Hautefeuille, K. Lebbou, C. Pédrini, D. Perrodin, and O. Tillement, IEEE Trans. Nucl. Sci. **NS-54** (2007) 391-397.
- [10] A. M. K. Foudray, F. Habte, C. S. Levin, and P. D. Olcott, IEEE Trans. Nucl. Sci. **NS-53** (2006) 2549-2556.
- [11] A. J. Chaudhari, Yongfeng Yang, R. Farrell, P. A. Dokhale, K. S. Shah, S. R. Cherry, and R. D. Badawi, IEEE Trans. Nucl. Sci. **NS-55** (2008) 853-861.
- [12] S. Aogaki, F. Takeuchi, IEEE Trans. Nucl. Sci. **NS-57** (2010) 1502-1511.
- [13] R. Brun, Available: <http://root.cern.ch/>
- [14] Available: <http://rcwww.kek.jp/research/egs/>
- [15] C. S. Levin, and E. J. Hoffman, Phys. Med. Biol. **44** (1999) 781-799.
- [16] A. Gorin, S. Horikawa, K. Kuroda, I. Manuilov, K. Okada, A. Ryazantsev, A. Siderov, and F. Takeuchi, Nucl. Instr. Meth. A **566** (2006) 500-515.